

# Spinning superfluid helium-4 nanodroplets

Francesco Ancilotto,<sup>1,2</sup> Manuel Barranco,<sup>3,4,5</sup> and Martí Pi<sup>3,4</sup>

<sup>1</sup>*Dipartimento di Fisica e Astronomia “Galileo Galilei” and CNISM,  
Università di Padova, via Marzolo 8, 35122 Padova, Italy*

<sup>2</sup>*CNR-IOM Democritos, via Bonomea, 265 - 34136 Trieste, Italy*

<sup>3</sup>*Departament FQA, Facultat de Física, Universitat de Barcelona. Diagonal 645, 08028 Barcelona, Spain*

<sup>4</sup>*Institute of Nanoscience and Nanotechnology (IN2UB), Universitat de Barcelona, Barcelona, Spain.*

<sup>5</sup>*Université Toulouse 3 and CNRS, Laboratoire des Collisions, Agrégats et Réactivité,  
IRSAMC, 118 route de Narbonne, F-31062 Toulouse Cedex 09, France*

(Dated: December 2, 2021)

We have studied spinning superfluid  $^4\text{He}$  nanodroplets at zero temperature using Density Functional theory. Due to the irrotational character of the superfluid flow, the shapes of the spinning nanodroplets are very different from those of a viscous normal fluid drop in steady rotation. We show that when vortices are nucleated inside the superfluid droplets, their morphology, which evolves from axisymmetric oblate to triaxial prolate to two-lobed shapes, is in good agreement with experiments. The presence of vortex arrays confers to the superfluid droplets the rigid-body behavior of a normal fluid in steady rotation, and this is the ultimate reason of the surprising good agreement between recent experiments and the classical models used for their description.

## I. INTRODUCTION

When a drop made of a normal liquid rotates, centrifugal forces produce deformations which change its spherical appearance at rest into an oblate, axisymmetric shape. If the drop spins fast enough, it may eventually distort into a two-lobed, peanut-shaped form before undergoing fission when it is no longer able to sustain the strain due to its own rotational motion. Hydrodynamical models aiming at describing rotating fluid drops have been successfully applied to systems that range from atomic nuclei to celestial objects. Most theoretical models assume the liquid to be incompressible and viscous so that drops eventually reach a steady state in which they rotate as if they were rigid bodies.<sup>1–10</sup>

Using wax samples under diamagnetic levitation, the theoretical shapes of rotating drops were reproduced experimentally.<sup>9</sup> This study has provided direct experimental validation of numerical models used to calculate equilibrium shapes of spinning drops made of classical fluids. With increasing angular momentum, the shapes of the wax samples progress from spheres (not rotating) to oblate-like shapes, to tri-axial shapes (three unequal axes), and finally to two-lobed (dumbbell) shapes. In the latter case the axis of rotation is perpendicular to the line joining the centers of the two lobes. For all shapes, the shortest axis always coincides with the axis of rotation.

With the experimental realization of superfluid helium drops using cryogenic free-jet gas expansions,<sup>11</sup> attention has been focused recently on the shapes of superfluid drops. It is commonly accepted that helium drops created in the normal, non-superfluid phase, may acquire angular momentum during the passage of the fluid through the nozzle of the experimental apparatus.<sup>12</sup> Vorticity, defined in hydrodynamics as  $\nabla \times \mathbf{v}$ ,<sup>13</sup> where  $\mathbf{v}$  is the velocity field of the fluid, is distributed inside the drop in the normal phase. It equals  $2\omega$  for a rotating rigid body, or for a viscous fluid in steady rotation,  $\omega$

being the angular velocity about the rotation axis.

During the expansion process the helium drops cool down to about 0.4 K temperature; at this temperature, the helium is superfluid and the normal fluid fraction is negligible. The spinning superfluid drops retain a large yet unknown fraction of the angular momentum deposited in them when they are still in the normal phase. Since the superfluid flow is irrotational,  $\nabla \times \mathbf{v} = 0$ , the vorticity remaining in the drops is concentrated in the cores of the quantized vortices nucleated in the drop interior<sup>14,15</sup> and in capillary waves.<sup>15,16</sup> This is the mechanism by which angular momentum is conserved in an isolated helium drop undergoing a normal to superfluid state transition.

Superfluid  $^4\text{He}$  drops in fast rotation have been studied by coherent x-ray scattering.<sup>17</sup> The shapes of the drops observed were consistent with those of axisymmetric oblate pseudo-spheroids with large aspect ratio, defined as the ratio of the long half-axis length to the short half-axis length along the rotational axis. The existence of vortex arrays inside a number of drops was established by the appearance of Bragg patterns from Xe clusters trapped in the vortex cores.<sup>17,18</sup> Doping the drops was instrumental for detecting the presence of vortices, the extremely small size of the vortex cores preventing their direct detection. At variance, the shapes of the drops could be instead inferred in the absence of doping.

While normal fluid drops change their shape as rotation becomes faster to resemble a “peanut” (two-lobe shape) or a “blood cell”,<sup>1,3,7</sup> no evidence of such shape shifting was seen in the experiments of Ref. 17. Density Functional Theory (DFT) calculations carried out for droplets containing 15000  $^4\text{He}$  atoms and up to  $n_v = 9$  vortices, confirmed the above scenario,<sup>19,20</sup> the comparison with the experimental measurements being facilitated by using suitably rescaled units to characterize the droplet shapes (see below), which showed indeed remarkable similarities with the experimental drops. Quite a

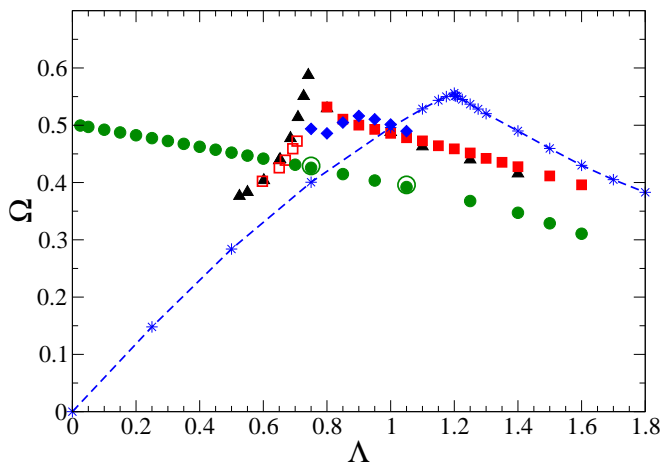


FIG. 1: Rescaled angular velocity  $\Omega$  vs. rescaled angular momentum  $\Lambda$ . Black triangles: 3-vortex configurations. Red squares: 4-vortex configurations (open, oblate-like; solid, linear). Blue diamonds: 4-vortex cross configurations. Green dots: vortex-free configurations; big empty green dots show values for the  ${}^4\text{He}_{5000}$  droplet. The blue starred symbols connected by a dashed line are the classical rotating drop results of Ref. 8.

few helium droplets displaying prolate shapes were subsequently identified in these small-angle, x-ray diffraction experiments.<sup>12</sup> So far, no theoretical analysis of the prolate configurations found in the experiments has been carried out. This is one of the purposes of the present work.

Very recently, coherent diffractive imaging experiments of rotating  ${}^4\text{He}$  drops using extreme ultraviolet pulses in conjunction with wide-angle x-ray diffraction have allowed to identify, in addition to oblate shapes, a large number of prolate shapes.<sup>21,22</sup> These experiments have been analyzed by simulating the observed diffraction patterns obtained from a simple parametrization model for the drop geometry (a combination of two ellipsoidal caps smoothly connected by a hyperboloidal centerpiece), and comparing them with the actual diffraction patterns until a match is found.

Comparison of the parametrized shapes of the experimental drops with those predicted by numerical calculations for normal liquid rotating drops<sup>9</sup> has shown a good agreement,<sup>22</sup> indicating that helium drops formed in the free jet expansion follow closely the sequence of shapes characteristic of normal fluid drops.

The most natural question arises, i.e. why spinning superfluid  ${}^4\text{He}$  drops, whose hydrodynamical hallmark is irrotational flow, behave instead as rotating normal liquid drops. The answer, as we will quantitatively show in the following, is that the presence of vortex arrays in the helium drops makes them behave as classical rotating liquid droplets.

The similarity between rotating superfluid  ${}^4\text{He}$  and the rigid-body rotation of a viscous liquid has been noted long ago for bulk  ${}^4\text{He}$  in a rotating bucket: in spite of

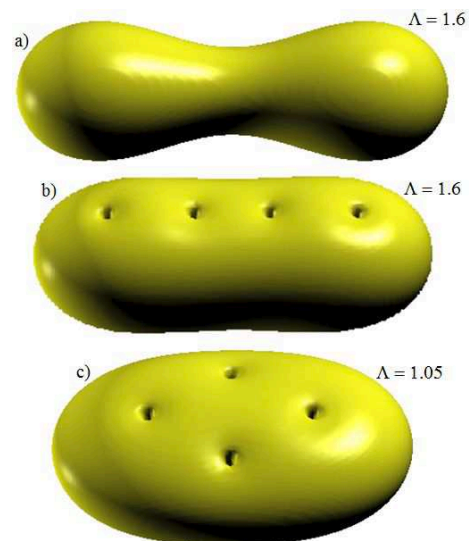


FIG. 2: Prolate  ${}^4\text{He}_{1500}$  droplet shapes (not to scale) represented by their sharp density surfaces and  $\Lambda$  values. a) Vortex-free configuration; b) 4-vortex linear configuration; c) 4-vortex cross configuration. The rotational axis coincides with the vertical axis in the figure.

its irrotational flow,  ${}^4\text{He}$  develops a meniscus just like a rotating normal fluid, instead of remaining at rest with a flat liquid-vapor interface.<sup>23</sup> This apparently contradictory behavior has been attributed to the nucleation of quantized vortices which carry most of the angular momentum of the rotating fluid.<sup>24</sup>

## II. METHOD

We have used Density Functional Theory to describe superfluid helium droplets.<sup>25</sup> Within DFT, the total energy of a  ${}^4\text{He}_N$  droplet at zero temperature is written as a functional of a complex effective wave function  $\Psi(\mathbf{r})$  related to its atomic density by  $\rho(\mathbf{r}) = |\Psi(\mathbf{r})|^2$ .

The droplet equilibrium configuration is obtained by solving the equation

$$\left\{ -\frac{\hbar^2}{2m_{\text{He}}} \nabla^2 + \frac{\delta \mathcal{E}_c}{\delta \rho} \right\} \Psi(\mathbf{r}) \equiv \mathcal{H}[\rho] \Psi(\mathbf{r}) = \mu_4 \Psi(\mathbf{r}) \quad (1)$$

where  $\mu_4$  is the  ${}^4\text{He}$  chemical potential and  $\mathcal{E}_c[\rho]$  is the correlation energy, for which we have taken that proposed in Ref. 26. This functional is finite-range and includes non-local effects. Both aspects are needed to describe quantitatively the response of the liquid at the  $\text{\AA}$ -scale. Unless explicitly stated, the number of helium atoms in the studied droplets is  $N = 1500$ .

To investigate non-zero angular momentum configurations in the spinning droplet it is convenient to move to the fixed-droplet frame of reference (corotating frame) by imposing, through the use of a Lagrange multiplier  $\omega$ , a fixed value for the total angular momentum  $\langle L_z \rangle$ , i.e. we

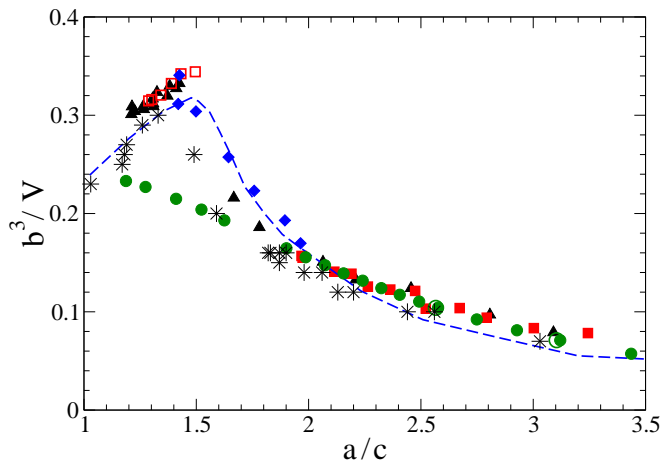


FIG. 3: Aspect-ratio  $b^3/V$  vs.  $a/c$  curve. Black triangles: 3-vortex configurations. Red squares: 4-vortex configurations (open, oblate-like; solid, linear). Blue diamonds: 4-vortex cross configurations. Green dots: vortex-free configurations; big empty green dots show values for the  ${}^4\text{He}_{5000}$  droplet. The black starred symbols show the experimental results of Ref. 22. The blue dashed line shows the classical rotating drop results of Ref. 9.

look for solutions of the equation

$$\{\mathcal{H}[\rho] - \omega \hbar \hat{L}_z\} \Psi(\mathbf{r}) = \mu_4 \Psi(\mathbf{r}) \quad (2)$$

where  $\hat{L}_z$  is the dimensionless angular momentum operator. The results presented in this work have been obtained using the 4He-DFT BCN-TLS computing package.<sup>27</sup> Details on how Eqs. (1) and (2) are solved can be found in Ref. 25 and references therein. We work in 3D cartesian coordinates and no symmetry is imposed to the solution of Eq.(2) during the functional minimization.

As in previous studies,<sup>6,8,12</sup> we use here rescaled units for angular momentum,  $\Lambda$ , and angular velocity,  $\Omega$ . This allows to compare our results, which are obtained for droplets made of  $O(10^3)$  atoms, with experimental results on large drops, made of  $10^8 - 10^{11}$  atoms. Such units are defined as<sup>28</sup>

$$\begin{aligned} \Omega &\equiv \sqrt{\frac{m_{\text{He}} \rho_0 R^3}{8\gamma}} \omega \\ \Lambda &\equiv \frac{\hbar}{\sqrt{8\gamma R^7 m_{\text{He}} \rho_0}} L_z \end{aligned} \quad (3)$$

where  $\gamma = 0.274 \text{ K } \text{\AA}^{-2}$  and  $\rho_0 = 0.0218 \text{ \AA}^{-3}$  are the surface tension and liquid atom density at zero temperature and pressure;  $R = 2.22 N^{1/3} \text{ \AA}$  is the sharp radius of the spherical droplet with  $N$  helium atoms and zero angular momentum, defined such that  $4\pi R^3 \rho_0 / 3 = N$ . Liquid helium is fairly incompressible and hence the volume of any deformed configurations can be safely identified with  $V = 4\pi R^3 / 3$ .

We have employed two different, alternative strategies to solve Eq. (2), i.e. we either (i) fix  $\omega$  and find the

associated stationary configuration, which will be characterized by some value of the angular momentum  $L_z$  depending upon the chosen value of  $\omega$ , or (ii) solve Eq. (2) by imposing a given value for  $L_z$  and iteratively find the associated value of  $\omega$ . Classically, the fixed  $\omega$  calculations correspond to forced rotation conditions (“driven drops”), while the fixed  $L_z$  calculations correspond to torque free drops with an initial prescribed rotation (“isolated drops”).<sup>3,5</sup> As shown in Ref. 3, it turns out that stable prolate configurations can only be found fixing the value of  $L_z$ . At variance, stable oblate configurations can be found either by fixing  $\omega$  or  $L_z$ .

### III. RESULTS

The  $\Omega(\Lambda)$  relationship for normal fluid drops in steady rotation is plotted with a dashed line in Fig. 1.<sup>8</sup> Configurations with  $\Lambda \lesssim 1.2$  have oblate axisymmetric shapes, and configurations with larger  $\Lambda$  values have prolate triaxial or two-lobed shapes;<sup>3,4,6,8</sup> the classical bifurcation point is at  $(\Lambda, \Omega) \sim (1.2, 0.56)$ .<sup>28</sup>

As shown also in Fig. 1, the calculated  $\Omega(\Lambda)$  relation for a superfluid droplet (filled dots) is very different. In this case, only prolate triaxial configurations may exist since axisymmetric oblate configurations are quantum mechanically forbidden.<sup>29</sup> The finite value of  $\Omega$  at very small values of  $\Lambda$  is the equivalent of the “rotational Meissner effect” occurring when liquid helium in a rotating cylinder is cooled through the lambda point: at sufficiently slow rotational speeds the superfluid forms in a state of zero total angular momentum, causing the container to rotate faster.<sup>30</sup> A nearly spherical configuration with a high value of  $\Omega$  and a negligible value of  $\Lambda$  can be seen for instance in Fig. 8 of Ref. 20.

The two empty circles in Fig. 1 have been calculated using a  $N = 5000$  droplet (see also Fig. 3). The purpose of these calculations has been to check explicitly the scaling of the results with the number of atoms in the droplet. A prolate vortex-free configuration corresponding to  $\Lambda = 1.6$  is shown in Fig. 2.

To allow for a sensible comparison with the experimental<sup>22</sup> and classical<sup>9</sup> results, we have determined the aspect ratio of the superfluid droplets. For any stationary configuration obtained solving Eq. (2), a sharp density surface is defined by calculating the locus at which the helium density equals  $\rho_0/2$ ; for a spherical distribution this corresponds to a sphere of radius  $R$ . In the case of deformed droplets, three lengths  $a, b, c$  are introduced representing the distances from the droplet center of mass to the sharp surface along the principal axis of inertia. Following the notation used in the experiments and in the classical models, we will take  $a$  and  $c$  as the largest and smallest radii, respectively. For an axisymmetric droplet  $a = b \neq c$ , whereas  $a \neq b \neq c$  in the case of triaxial, prolate shapes.

Figure 3 displays  $b^3/V$  vs. the ratio  $a/c$ ; when  $a/c = 1$ ,  $b^3/V = R^3/V = 3/(4\pi)$ . The dashed line and the starred

symbols show the classical model and the experimental results, respectively, while the filled dots correspond to superfluid-droplet DFT calculations. We recall here that all the superfluid droplets corresponding to the filled dots are prolate. As for the  $\Omega(\Lambda)$  curve in Fig. 1, it may be seen that the rotational normal fluid and the irrotational superfluid results are very different for low and intermediate values of the angular momentum (corresponding to low-to-intermediate values of  $a/c$  in Fig. 3), and they also differ from the experimental results in the same range. It is worth stressing here that, at variance with the classical rotating droplet case, where the rotational axis always coincides with the shortest ( $c$ ) axis, for superfluid droplets the opposite is true, i.e. the rotational axis coincides instead with the intermediate ( $b$ ) axis.

The discrepancy between our results and the experimental ones is particularly striking in the region  $a/c < 1.5$ , where oblate-like shapes are experimentally found. We observe at this point that oblate-like configurations can only store angular momentum by nucleating a number of vortices in their interior, in the form of a vortex array that reduces the  $D_{\infty h}$  symmetry of the axisymmetric vortex-free droplet to, e.g., a  $D_{nh}$  symmetry if  $n$  vortices are evenly distributed in a ring around the droplet center. Examples of oblate-like configurations hosting a different number of vortices have been presented in Ref. 19.

We have thus calculated the equilibrium shapes of rotating  $^4\text{He}$  droplets hosting vortices solving also Eq. (2), this time using the imprinting procedure<sup>19,25</sup> by which  $n_v$  vortex lines parallel to the  $z$  axis are initially created. This is achieved by starting the iterative solution of Eq.(2) from the effective wave function

$$\Psi_0(\mathbf{r}) = \rho_0^{1/2}(\mathbf{r}) \prod_{j=1}^{n_v} \left[ \frac{(x - x_j) + i(y - y_j)}{\sqrt{(x - x_j)^2 + (y - y_j)^2}} \right] \quad (4)$$

where  $(x_j, y_j)$  is the initial position of the  $j$ -vortex linear core with respect to the  $z$ -axis of the droplet, and  $\rho_0(\mathbf{r})$  is the vortex-free droplet density profile. The initial vortex positions are guessed and during the functional minimization of the total energy, both the vortex positions and droplet density are allowed to change to provide at convergence the lowest energy configuration for the chosen value of  $\omega$  or  $L_z$ .

In this case, part of the angular momentum of the droplet is stored in vortices and part in capillary waves, always present in prolate configurations. Indeed, for oblate configurations one has  $L_z \lesssim n_v N \hbar$  with  $n_v = 1, 2, \dots$ , whereas for most prolate configurations  $L_z > n_v N \hbar$ , the extra angular momentum being associated to capillary waves.

Figure 2 displays one of such prolate configuration hosting  $n_v = 4$  vortices for  $\Lambda = 1.6$ . This  $n_v$  is the largest number of vortices the  $N = 1500$  atoms droplet may accommodate. Depending upon the value of  $\Lambda$ , the vortex cores can be either arranged in a cross-like configuration (stable at low values of  $\Lambda$ ) or aligned along the

largest droplet axis (stable at high values of  $\Lambda$ ). Fig. 2 also displays a prolate droplet hosting four vortices in a cross configuration for  $\Lambda = 1.05$ .<sup>31</sup> Notice that the vortex cores meet the droplet surface perpendicularly.

We display in Fig. 1 the  $\Omega(\Lambda)$  relationship for the droplets hosting  $n_v = 3$  and 4 vortices. The resulting curve is compared with the classical model predictions.<sup>9</sup> Note that, similarly to the classical case, a bifurcation point appears, separating the oblate droplets configurations (left branch) from the prolate droplets ones (right branch). The difference between the vortex-hosting droplets case and the vortex-free droplets (green dots) shows how different is the way in which angular momentum is stored in the two cases.

The  $b^3/V$  vs.  $a/c$  curve in the presence of vortices now displays a rising branch in the left part of the aspect-ratio curve of Fig. 3 corresponding to oblate-like configurations, in agreement with experiments and classical calculations. Remarkably, the oblate-like part of that curve stops close to the value  $a/c = 1.5$ , which is the classical stability limit for axisymmetric configurations.<sup>1</sup> Nearly from this  $a/c$  value on, the stationary configurations have prolate shapes. We display in Fig. 3 (as well as in Fig. 1) results for both 4-vortex cross and linear configurations at  $\Lambda$  values where they are both stable; according to our calculations, cross and linear configurations with the same value of  $\Lambda$  are nearly degenerate and could both be realized in the experiments.

#### IV. DISCUSSION AND CONCLUSIONS

Figure 3 contains the key results of the present study, that we summarize as follows:

- The predicted shapes of vortex-free superfluid droplets (green dots in Fig. 3) are much different from the experimental results<sup>21,22</sup> in the region of the aspect-ratio chart characterized by low-medium values of  $a/c$  (corresponding to low-medium values of  $\Lambda$ ), while they agree in the region of higher  $a/c$  values (corresponding to higher  $\Lambda$ ).
- The presence of vortices drastically modify the sequence of permitted droplet shapes, in particular allowing the appearance of stable axisymmetric (oblate-like) shapes, in agreement with experiments. Given the way they are produced, there is no reason why  $^4\text{He}$  drops should not host a number of vortices, possibly created via the Kibble-Zurek mechanism,<sup>32</sup> as it happens in liquid  $^4\text{He}$  where a fast adiabatic passage through the lambda transition results in copious vortex production.<sup>33</sup>
- Our calculations show that when the number of vortices in the droplet is close to its maximum possible (four in the case of the small droplet used in the DFT calculations), the aspect-ratio  $b^3/V$  vs.  $a/c$  curve agrees with that obtained using the classical rotating droplet model. Some differences are expected to show up between both approaches, as drops in classical models are considered

incompressible and the existence of any surface width is neglected, whereas within DFT liquid compressibility and surface width are taken into account. From the overall good agreement between experiments and classical models of rotation regarding the droplet morphology,<sup>21,22</sup> one can infer that the droplets observed in experiments host quantized vortices whose presence could be determined after doping them.<sup>17,18</sup> Our results also show that vortex arrays are naturally present in prolate droplets, instead of just being associated with oblate-like helium droplets as it is commonly believed.

- Prolate vortex-free helium droplets are also stable objects in which the angular momentum is stored as giant capillary waves (like those reported on charged helium drops levitated with a magnetic field<sup>16</sup>). Such droplets can achieve much larger values of  $a/c$  than those hosting vortices. In particular, we have found stable configurations for  $a/c$  as large as 4.5, whereas the largest  $a/c$  values displayed in Fig. 3 for the droplets hosting vortices correspond to their actual stability limit. According to our results, vortex-free droplets shapes are indistinguishable from droplets hosting vortices unless the rotational axis is identified in the experiments, whereas they could be currently detected and distinguished from vortex-hosting ones in the range  $1 < a/c \lesssim 1.6$ . However, they have apparently escaped direct measure so far (there is only one point with  $a/c \sim 1.6$  in the experimental aspect ratios that could be a potential candidate, see Fig. 3), because they likely constitute a fairly small fraction of the –already small– fraction of deformed drops identified in the experiments (the majority of the imaged <sup>4</sup>He drops are spherical, only about 1.5 % of those of Ref. 22 showed diffraction patterns corresponding to prolate-like deformed shapes), making difficult their direct detection.

Finally, we comment briefly on the relative stability of

configurations having a different number of vortices  $n_v$  for a given value of  $\Lambda$ . Obviously, only one of the  $n_v$  values corresponds to the globally stable configuration, the others can only be metastable. It might be that these configurations are separated by energy barriers whose existence cannot be determined by the present method, as it only yields the lowest energy configuration for a fixed  $L_z$  and a chosen  $n_v$ . However, according to our calculations, these configurations differ in energy by less than 1% and it cannot be discarded that they all might show up in the experiments. A full analysis of the morphology of the droplets and their stability as a function of  $n_v$  goes beyond the scope of the present work and it is not even necessary for discussing the current experimental results. In fact, the calculated structures of droplet hosting vortices lie along a common aspect ratio curve, as Fig. 3 clearly shows, and even if some of the calculated points represent metastable states, the main conclusions of our work will not change.

### Acknowledgments

We thank Jordi Boronat, Andrey Vilesov, Sam Butler, Thomas Möller, and Bruno Langbehn for useful discussions and exchanges. We are most indebted to Thomas Möller and Bruno Langbehn for sharing with us their experimental results, and to Sam Butler for providing us with the results of the classical model calculations. This work has been performed under Grant No FIS2017-87801-P from DGI (Spain). MB thanks the Université Fédérale Toulouse Midi-Pyrénées for financial support throughout the “Chaires d’Attractivité 2014” Programme IMDYNHE.

- 
- <sup>1</sup> S. Chandrasekhar, Prog. R. Soc. Lond. A **286**, 1 (1965).
  - <sup>2</sup> S. Cohen, R. Plasil, and W.J. Swiatecki, Ann. Phys. **82**, 557 (1974).
  - <sup>3</sup> R.A. Brown and L.E. Scriven, Proc. R. Soc. Lond. A **371**, 331 (1980).
  - <sup>4</sup> R.A. Brown and L.E. Scriven, Phys. Rev. Lett. **45**, 180 (1980).
  - <sup>5</sup> A.K. Nurse, S.R. Coriell, and G.B. McFadden, J. Res. Natl. Inst. Stan. **120**, 74 (2015).
  - <sup>6</sup> C.-J. Heine, IMA J. Num. Anal. **26**, 723 (2006).
  - <sup>7</sup> R.J.A. Hill and L. Eaves, Phys. Rev. Lett. **101**, 234501 (2008).
  - <sup>8</sup> S.L. Butler, M.R. Stauffer, G. Sinha, A. Lilly, and R.J. Spiteri, J. Fluid Mech. **667**, 358 (2011).
  - <sup>9</sup> K.A. Baldwin, S.L. Butler, and R.J.A. Hill, Sci. Rep. **5**, 7660 (2015).
  - <sup>10</sup> L. Liao and R.J.A. Hill, Phys. Rev. Lett. **110**, 114501 (2017).
  - <sup>11</sup> J.P. Toennies and A.F. Vilesov, Angew. Chem. Phys. **43**, 2622 (2004).
  - <sup>12</sup> C. Bernando, R.M.P. Tanyag, C. Jones, C. Bacellar, M. Bucher, K.R. Ferguson, D. Rupp, M. P. Ziemkiewicz, L.F. Gomez, A.S. Chatterley, T. Gorkhover, M. Müller, J. Bozek, S. Carron, J. Kwok, S.L. Butler, T. Möller, Ch. Bostedt, O. Gessner, and A.F. Vilesov, Phys. Rev. B **95**, 064510 (2017).
  - <sup>13</sup> E. Guyon, J.-P. Hulin, L. Petit, and C.D. Matescu, *Physical Hydrodynamics*, 2nd. ed., Oxford University Press, Oxford, U.K., 2015.
  - <sup>14</sup> R.J. Donnelly, *Quantized vortices in helium II*, Cambridge Studies in Low Temperature Physics, Cambridge University Press, Cambridge, U.K. 1991, Vol. 3.
  - <sup>15</sup> A.L. Fetter, J. Low Temp. Phys. **16**, 533 (1974).
  - <sup>16</sup> D.L. Whitaker, M.A. Weilert, C.L. Vicente, H.J. Maris, and G.M. Seidel, J. Low Temp. Phys. **110**, 173 (1998).
  - <sup>17</sup> L.F. Gomez, K.R. Ferguson, J.P. Cryan, C. Bacellar, R.M.P. Tanyag, C. Jones, S. Schorb, D. Anielski, A. Belkacem, C. Bernando, R. Boll, J. Bozek, S. Carron, G. Chen, T. Delmas, L. Englert, S.W. Epp, B. Erk, L. Foucar, R. Hartmann, A. Hexemer, M. Huth, J. Kwok, S.R. Leone, J.H. S. Ma, F.R. N. C. Maia, E. Malmerberg, S. Marchesini, D.M. Neumark, B. Poon, J. Prell, D. Rolles, B.

- Rudek, A. Rudenko, M. Seifrid, K.R. Siefermann, F.P. Sturm, M. Swiggers, J. Ullrich, F. Weise, P. Zwart, C. Bostedt, O. Gessner, and A.F. Vilesov, *Science* **345**, 906 (2014).
- <sup>18</sup> C.F. Jones, C. Bernando, R.M.P. Tanyag, K.R. Ferguson, C. Bacellar, L. Gomez, D. Anielski, A. Belkacem, R. Boll, J. Bozek, S. Carron, J. Cryan, L. Englert, S.W. Epp, B. Erk, R. Hartmann, L. Foucar, D.M. Neumark, D. Rolles, B. Rudek, A. Rudenko, K.R. Siefermann, F.P. Sturm, J. Ullrich, F. Weise, Ch. Bostedt, O. Gessner, and A.F. Vilesov *Phys. Rev. B* **93**, 180510(R) (2016).
- <sup>19</sup> F. Ancilotto, M. Pi and M. Barranco, *Phys. Rev. B* **91**, 100503(R) (2015).
- <sup>20</sup> F. Coppens, F. Ancilotto, M. Barranco, N. Halberstadt, and M. Pi, *Phys. Chem. Chem. Phys.* **19**, 24805 (2017).
- <sup>21</sup> D. Rupp, N. Monserud, B. Langbehn, M. Sauppe, J. Zimmermann, Y. Ovcharenko, T. Möller, F. Frassetto, L. Polletto, A. Trabattini, F. Calegari, M. Nisoli, K. Sander, C. Peltz, M. J. J. Vrakking, T. Fennel, and A. Rouzee, *Nature Commun.* **8**, 493 (2017).
- <sup>22</sup> B. Langbehn, K. Sander, Y. Ovcharenko, C. Peltz, A. Clark, M. Coreno, R. Cucini, P. Finetti, M. Di Fraia, L. Giannessi, C. Grazioli, D. Iablonskyi, A.C. LaForge, T. Nishiyama, V. Oliver Álvarez de Lara, P. Piseri, O. Plekan, K. Ueda, J. Zimmermann, K.C. Prince, F. Stienkemeier, C. Callegari, T. Fennel, D. Rupp, and T. Möller, arXiv:1802.10584
- <sup>23</sup> D.V. Osborne, *Proc. Phys. Soc. A* **63** 909 (1950).
- <sup>24</sup> L. Pitaevskii and S. Stringari, *Bose-Einstein Condensation and Superfluidity*, International Series of Monographs on Physics vol. 164 Oxford University Press, 2016.
- <sup>25</sup> F. Ancilotto, M. Barranco, F. Coppens, J. Eloranta, N. Halberstadt, A. Hernando, D. Mateo, and M. Pi, *Int. Rev. Phys. Chem.* **36**, 621 (2017).
- <sup>26</sup> F. Ancilotto, M. Barranco, F. Caupin, R. Mayol, and M. Pi, *Phys. Rev. B* **72**, 214522 (2005).
- <sup>27</sup> 4He-DFT BCN-TLS: A Computer Package for Simulating Structural Properties and Dynamics of Doped Liquid Helium-4 Systems. M. Pi, F. Ancilotto, F. Coppens, N. Halberstadt, A. Hernando, A. Leal, D. Mateo, R. Mayol, and M. Barranco, <https://github.com/bcntls2016/>
- <sup>28</sup> We use the  $\Lambda$  definition of Refs.<sup>6,8,12</sup> that is four times larger than that of Refs.<sup>3,4</sup>.
- <sup>29</sup> F. Villars, *Ann. Rev. Nucl. Sci.* **7**, 185 (1957).
- <sup>30</sup> G.B. Hess and W.M. Fairbank, *Phys. Rev. Lett.* **19**, 216 (1967).
- <sup>31</sup> See Supplemental Material at [URL will be inserted by publisher] for other droplet shapes.
- <sup>32</sup> T.W.B. Kibble, *J. Phys. A* **9**, 1387 (1976); W.H. Zurek, *Nature* **317**, 505 (1985).
- <sup>33</sup> P.C. Hendry, N.S. Lawson, R.A.M. Lee, P.V.E. McClintock, and C.D.H. Williams, *J. Low Temp. Phys.* **93**, 1059 (1993).